Accepted Manuscript

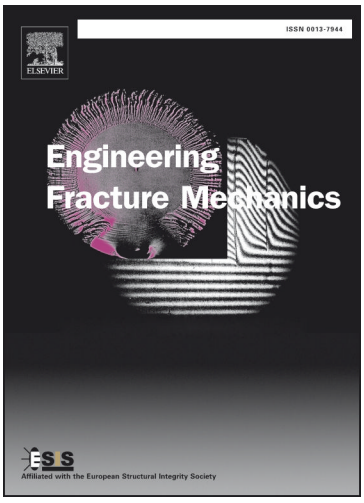

Simulation of Induced Acoustic Emission in Fractured Porous Media

M. Komijani, R. Gracie, E. Sarvaramini

PII: S0013-7944(18)30519-8
DOI: https://doi.org/10.1016/j.engfracmech.2018.07.028
Reference: EFM 6094

To appear in: *Engineering Fracture Mechanics*

Received Date: 17 May 2018
Revised Date: 18 July 2018
Accepted Date: 19 July 2018

Please cite this article as: Komijani, M., Gracie, R., Sarvaramini, E., Simulation of Induced Acoustic Emission in Fractured Porous Media, *Engineering Fracture Mechanics* (2018), doi: https://doi.org/10.1016/j.engfracmech.2018.07.028

Simulation of Induced Acoustic Emission in Fractured Porous Media

M. Komijani, R. Gracie*, E. Sarvaramini

Department of Civil and Environmental Engineering, University of Waterloo, Waterloo, Ontario, Canada

Abstract

Acoustic/microseismic Emissions (AE) in naturally fractured porous media are the result of local instability along internal interfaces and the sudden release of strain energy stored in the rock matrix. This rapid release of energy, stimulates high-frequency components of the dynamic response of the rock mass, inducing mechanical wave propagation. In this article an enriched finite element model is employed to concurrently simulate the interface instability and the induced wave propagation processes in a fractured porous media. Harmonic enrichment functions are used in the context of the Generalized Finite Element Method (GFEM) to suppress the spurious oscillations that can appear in wave propagation/dynamic modelings using regular finite elements. To model the fractures, the Phantom Node Method (PNM) is employed with the GFEM. The frictional contact condition at material interfaces is modeled using a stable augmented Lagrange multiplier approach. Through various parametric studies it's shown that i) decreasing the permeability leads to an increase in the frequency and a decrease in the amplitude of the acoustic signal; ii) increasing viscous damping leads to narrower frequency spectrum and decreased magnitude of the emitted acoustic signal; iii) increasing damping leads to a transition from transient wave propagation to diffusion-dominated AE response; iv) increasing interface friction leads to more pronounced stick-slip behavior and higher amplitude AE-without interface friction there is no AE. Lastly, the numerical illustrations demonstrate the superior capability of the enriched model (in comparison with regular finite element models) in suppressing the spurious oscillations in AE solutions.

Keywords:

Acoustic emission, Porous media, Fracture, Contact simulation, Generalized finite element method.

1. Introduction

The process of elastic wave propagation induced by an abrupt local release of stored strain energy is known as Acoustic Emission (AE) [1]. Acoustic emissions are generated by bifurcation-instabilities such as fault reactivation, pore collapse, and fracture, i.e., localization phenomena. As a result, AE monitoring

*Corresponding author. E-mail address: rgracie@uwaterloo.ca

and analysis are often used to probe the behaviour of solid materials in engineering applications such as, concrete structures [2, 3] and masonry bridges [4], and also geological formations, particularly in mining and hydraulic fracturing applications [5, 6]. For example, during hydraulic fracturing, microseismic monitoring is often conducted to determine the extent and orientation of the fracture network created [7]. A series of experimental and numerical investigations have been conducted by Carpinteri and his coworkers on analysis of damage and fracturing behaviour in solids and the associated induced acoustic emissions [8, 9, 10, 11]. These work demonstrate a correlation between acoustic events observed in experiments and microscale fracturing and damage processes. Analysis of acoustic emissions induced by localization is full of uncertainties and researchers have not yet focused on both explicitly modeling the fracturing/damage process and the simulation of associated induced acoustic wave propagation (specially in shear failure type). In this article, a specially designed enriched mixed-finite element model is employed to study both fracture reactivation due to hydraulic perturbations in a porous media and the resulting AEs. Using this model, the key system characteristics (e.g., friction, permeability, etc.) governing the nature of the emitted AEs are elucidated.

Recent attempts to correlate fracturing/slip and microseismic emission do not explicitly simulate transient acoustic wave propagation through the media following the release of elastic energy, e.g., Tang et al. [12, 13] used a quasi-static approach to relate the energy released by damage to the magnitude of acoustic events. Such approaches do not account for the propagation and interactions of emitted waves with discontinuities, attenuation, nor other wave reflection and coalescence phenomena.

Another class of acoustic emission simulation methods make use of the particle-based Discrete Element Method (DEM), in which the rock mass is represented as a collection of particles/blocks connected together by contact/cohesive forces. Localization and nucleation of fractures is modeled by breakage of the cohesive bonds between particles. Based on this methodology, Hazzard and Young [14] proposed a technique for the simulation of acoustic emission under nucleation (i.e., bond breakage) in rock. The radiated acoustic energy from the source was estimated by measuring the change in kinetic energy upon failure of the bond; however, wave emission and propagation were not directly simulated. In a similar fashion, Lisjak et al. [15] investigated acoustic emissions using DEM with non-porous deformable blocks, where AEs were related to an energy release through cohesive tension (not shear) tractions between blocks; while an explicitly time integrated dynamic model was used, the accuracy of the wave forms and wave propagation was not the focus of the study. It is important to note that most microseismicity induced in applications like hydraulic fracturing is due to shear failure and sliding along pre-existing discontinuities [16]. Other versions of DEM have also been proposed for studying acoustic emission signals induced by damage. For instance, Carpinteri and his

coworkers [17, 18] employed three-dimensional lattice models based on truss-like Discrete Element Method to study AEs in a prismatic concrete specimen subjected to compressional loads. They demonstrated good correlations between numerical results and AE data obtained from experimental tests.

There is a limited number of semi-analytical elastodynamics solution of AEs induced by sudden fracture nucleation, for example the models of Andreykiv et al. [19, 20, 21] for the AE due to the nucleation of penny-shaped fractures under modes I and III. None of the available analytical or semi-analytical solutions specifically address AE due to failure in shear (mode II) (i.e., microseismicity) under compression, where contact forces and frictional behaviour influence the AEs. Furthermore, there is a lack of solutions for AE in porous media due to reactivation of fracture or fracture nucleation.

Analysis of porous media spans applications from the geomechanics of reservoirs [22] to biomechanical analysis of tissues and cells [23, 24]. It is common in such models to assume that the fluid flow is transient but the solid evolves quasi-statically. There has been less emphasis on dynamic simulation of fracture in porous media; the focus to date has been on the modeling of fracture propagation rather than the simulation of the waves emitted from the cracks. For example, recently Cao et al. [25] simulated the stepwise process of fracturing in porous media and the associated fluid pressure oscillations using the standard FEM and Rethore et al. [26] modeled the dynamic propagation of shear bands in saturated porous media. However, these earlier works did not address the topic of simulation of wave propagation nor acoustic emission.

Accurate simulation of wave propagation using standard finite element approaches is problematic, as the polynomial basis functions used have been shown to be insufficient in some dynamic simulations [27]. Conventional finite element solutions of wave phenomena are well-known to contain spurious wave forms, which often cannot be efficiently eliminated using mesh refinement in transient and time-harmonic waves with short wave lengths [28]. Furthermore, numerical dispersions can significantly affect wave propagation velocity. Enriched Generalized Finite Element Methods (GFEM) have been developed to inhibit the spurious oscillations [29, 28]. Recently, Komijani and Gracie [30] extended these models to wave propagation in fractured media by combining the GFEM approach with the initial discretization-independent fracture/discontinuity modeling ability of the Phantom Node Method (PNM) of [31]. The enriched model (PNM-GFEM) combines the benefits of the two methods and minimizes the non-physical oscillations observed in regular dynamics simulations of fractures.

It is noted that in addition to the weak form-based finite element methods, a new class of numerical

methods, i.e., Extended Particle Difference Method (EPDM) [32, 33, 34], has been developed recently to model strong/weak discontinuities independently of the initial discretization, which may be used as an alternative for the finite element methods. The EPDM is a strong form-based numerical solution of the governing equations with the particle derivative approximation. In addition to the increase of computational efficiency that is achieved by avoiding numerical integration of the weak form, one of the notable features of the EPDM is that, unlike the weak form-based methods there is no need for employing an additional boundary tracking scheme such as the level set method. This makes the method very suitable for moving boundary problems.

This article presents the application of an extension of the PNM-GFEM method to acoustic wave emission simulation in fractured porous media. The media is modeled using mixture theory of poroelasticity [35, 36]. The solution of the governing system of equations is approximated using a mixed enriched finite element method (PNM-GFEM-M). The frictional contact at the interface of the fractures is simulated using an augmented Lagrange multiplier technique. Fracture instability is initiated via a perturbation source like fluid injection near the discontinuity, causing a stick to slip transition and leading to a sudden release of energy. Acoustic emissions, triggered through a sudden release of strain energy at the discontinuity interface due to shear failure, are simulated. It is shown that the PNM-GFEM-M results in more spurious-oscillation-free AEs compared to standard finite element approaches because it suppresses numerical dispersions of acoustic signals in both velocity and pore pressure fields. Using this simulation tool, the role of permeability, viscous damping, and contact friction on AEs is more clearly illustrated.

2. Mathematical Formulation

The differential equations governing the interaction of solid and fluid phases in porous media are obtained from Biot's mixture theory based on the concept of volume fractions for each phase.

2.1. Governing Equations

A two-dimensional poroelastic medium, Ω in Cartesian coordinate O_{xy} is considered. Let $\boldsymbol{u}(x, y, t)$ denote the displacement vector of the total mixture. For the sake of completeness, the well-established formulation of mixture theory of poroelasticity is given below.

The linear strain-displacement relation in infinitesimal deformation is

$$\boldsymbol{\varepsilon} = \frac{1}{2}(\nabla \boldsymbol{u} + (\nabla \boldsymbol{u})^T) \tag{1}$$

The constitutive equation for the solid matrix is given by:

$$\boldsymbol{\sigma'} = \boldsymbol{C} : \boldsymbol{\varepsilon} \tag{2}$$

in which $\boldsymbol{\sigma'}$ is the effective stress tensor acting on the solid skeleton, and $\boldsymbol{C}$ is the elastic stiffness tensor.

The relative motion of the fluid phase with respect to the total mixture is denoted by $w_i(x,t)$. To arrive at a two-field model, it is assumed that the relative acceleration of the fluid phase with respect to the total mixture is negligible, i.e., $\ddot{w}_i = 0$. This assumption has been shown to be appropriate for loading conditions up to earthquake frequencies for the saturated porous media [37, 41]. The momentum balance of the total mixture is:

$$\nabla \cdot \boldsymbol{\sigma} - \rho \ddot{\boldsymbol{u}} + \rho \boldsymbol{b} = 0 \tag{3}$$

in which $\ddot{\boldsymbol{u}}$ denotes the acceleration of the mixture, $\boldsymbol{\sigma}$ is the total stress, ρ is the average mixture density, and b is the body force acting on the mixture.

The average density of the mixture is defined as a weighted summation of solid and fluid phases densities

$$\rho = n'\rho_f + (1 - n')\rho_s \tag{4}$$

in which ρ_f and ρ_s are the density of fluid phase and solid skeleton, respectively, and n' is the porosity of the media.

The total stress of the mixture is defined as a combination of the stress acting on the solid phase and the pore pressure:

$$\boldsymbol{\sigma} = \boldsymbol{\sigma'} - \alpha_p p \boldsymbol{I} \tag{5}$$

where p is the fluid pore pressure, $\boldsymbol{I}$ is the identity tensor, $\boldsymbol{\sigma'}$ denotes the effective stress acting on the solid skeleton, and α_p is Biot's coefficient.

Neglecting the relative acceleration of the pore fluid with respect to the mixture, the generalized Darcy relation can be obtained from conservation of momentum of the fluid phase:

$$-\nabla p - \boldsymbol{R} - \rho_f \ddot{\boldsymbol{u}} + \rho_f \boldsymbol{b} = 0 \tag{6}$$

in which $\boldsymbol{R}$ is the averaged viscous drag force acting on the fluid defined by the Darcy seepage law:

$$\dot{\boldsymbol{w}} = \boldsymbol{k}_f \boldsymbol{R} \tag{7}$$

where $\boldsymbol{k}_f$ is the permeability tensor of the porous media.

The Eulerian continuity equation of the fluid phase can be written as:

$$\nabla \cdot \dot{\boldsymbol{w}} + \alpha \nabla \cdot \dot{\boldsymbol{u}} + \frac{\dot{p}}{Q} = 0 \tag{8}$$

in which $1/Q = (\alpha - n')/K_s + n'/K_f$, and K_s and K_f are the bulk moduli of solid and fluid phases, respectively.

The relative velocity of the fluid phase with respect to the mixture (i.e., $\boldsymbol{w}$) may be eliminated from (8) using (6) and (7) resulting in

$$\nabla \cdot k_f[-\nabla p - \rho_f \ddot{\boldsymbol{u}} + \rho_f \boldsymbol{b}] + \alpha \nabla \cdot \dot{\boldsymbol{u}} + \frac{\dot{p}}{Q} = 0 \tag{9}$$

Equations (3) and (9) are the governing differential equations of the problem for the unknown displacement and pore pressure fields[37].

2.2. Weak Formulation of the Governing Differential Equations

Consider a porous media Ω with boundary Γ. Boundary Γ comprises of Γ_u, Γ_t, Γ_p, and Γ_w, which represent the boundary surfaces for prescribed displacement, traction, pore pressure, and out-flow flux of fluid, respectively. Domain Ω contains internal interfaces denoted by Γ_d.

A weak formulation of the coupled system of equations (3) and (9) may be developed using appropriate test functions, $\delta\boldsymbol{u}$ and δp. The problem to be solved is to find $\mathbf{u}(x, y, t) \in U$ and $p(x, y, t) \in W$ such that

$$\int_\Omega \boldsymbol{\sigma} : \delta\boldsymbol{\varepsilon}\ d\Omega + \int_\Omega \rho \ddot{\boldsymbol{u}} \cdot \delta\boldsymbol{u}\ d\Omega - \int_{\Gamma_t} \bar{\boldsymbol{t}} \cdot \delta\boldsymbol{u}\ d\Gamma - \int_\Omega \rho \boldsymbol{b} \cdot \delta\boldsymbol{u}\ d\Omega + \int_{\Gamma_d} \bar{\boldsymbol{t_d}} \cdot \delta[[\boldsymbol{u}]]\ d\Gamma = 0, \forall \delta\boldsymbol{u} \in U_0 \tag{10}$$

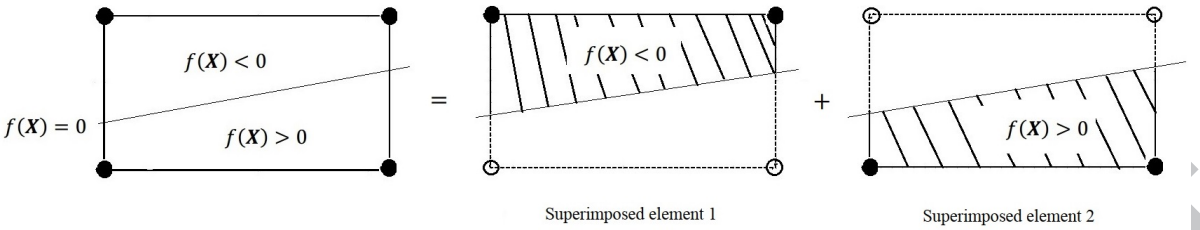

Figure 1: Decomposition of a cracked element into two superimposed paired elements with original real and additional phantom nodes in the PNM. Original real nodes and additional phantom nodes are shown by solid and hollow circles, respectively. The shaded region of each superimposed element represents the active portion of those elements.

$$\int_\Omega \nabla\delta p \cdot k_f \nabla p \; d\Omega + \int_\Omega \nabla\delta p k_f \cdot \rho_f \ddot{\boldsymbol{u}} \; d\Omega + \int_\Omega \delta p \; \alpha_p \; \nabla \cdot \dot{\boldsymbol{u}} \; d\Omega + \int_\Omega \delta p \; 1/Q \; \dot{p} \; d\Omega -$$
$$\int_\Omega \nabla\delta p k_f \cdot \rho_f \boldsymbol{b} \; d\Omega + \int_{\Gamma_w} \delta p (\dot{\boldsymbol{w}} \cdot \boldsymbol{n}_\Gamma) \; d\Gamma - \int_{\Gamma_d} \delta p [[\dot{\boldsymbol{w}}]] \cdot \boldsymbol{n}_{\Gamma_d} \; d\Gamma = 0, \forall \delta p \in W_0 \tag{11}$$

in which U,W, U_0, and W_0 are appropriate function spaces. The jump in the displacement field across the discontinuity surface is denoted by $[[\boldsymbol{u}]]$, and $[[\dot{\boldsymbol{w}}]]$ is the discontinuity of fluid flux into the crack interface from either crack face. $\bar{\boldsymbol{t}}_{\boldsymbol{d}}$ denotes the internal applied traction (e.g., contact force) on the internal discontinuity Γ_d.

3. Finite Element Formulation

3.1. Mixed GFEM-enriched Phantom Node Method (PNM-GFEM-M)

To model a discontinuity in the displacement and pore pressure fields within a fractured element, the Phantom Node Method (PNM) [31] is employed to achieve a discontinuous interpolation of the fields. This is accomplished using two superimposed paired elements with original real and additional fictitious/phantom nodes. In this framework, each element cut by a crack is replaced by two superimposed continuous elements with real and additional phantom nodes, as shown schematically in Figure 1. Despite their name, phantom nodes, are real nodes of the finite element mesh and as such have their own displacement and pressure degrees of freedom. Each of the superimposed elements are divide by the fracture into active and inactive parts. The active part of each superimposed element models a different side of the fracture. Also, based on the general idea of PNM-GFEM method [30], trigonometric enrichment basis functions [28] are used to enrich the approximation functions to suppress the non-physical numerical dispersions that can appear in dynamic response of regular FEM solutions.

3.1.1. Displacement field discretization

For a cracked element in a porous media, the PNM-GFEM [30] interpolation is employed to approximate the displacement in the x and y directions, i.e.,

$$u_x(x,y,t) = H(-f(x,y)) \sum_{I\in S_1} \Big(\boldsymbol{\psi}_I^1(x,y)\boldsymbol{u}_{Ix}(t)\Big) + H(f(x,y)) \sum_{I\in S_2} \Big(\boldsymbol{\psi}_I^1(x,y)\boldsymbol{u}_{Ix}(t)\Big) \tag{12}$$

$$u_y(x,y,t) = H(-f(x,y)) \sum_{I\in S_1} \Big(\boldsymbol{\psi}_I^2(x,y)\boldsymbol{u}_{Iy}(t)\Big) + H(f(x,y)) \sum_{I\in S_2} \Big(\boldsymbol{\psi}_I^2(x,y)\boldsymbol{u}_{Iy}(t)\Big) \tag{13}$$

in which $H(\cdot)$ is the step function and S_1 and S_2 are the sets of nodes corresponding to each of the two superimposed elements. Each of the two superimposed elements contains original real nodes and additional phantom nodes. The location of the discontinuity inside an element is defined by a level set function such that $f(x,y)=0$ specifies the discontinuous surface. $\boldsymbol{\psi}_I^1$ and $\boldsymbol{\psi}_I^2$ are the arrays of conventional and enriched basis functions of node I for the displacement components in x and y directions, respectively. Vectors of corresponding conventional and enriched displacement degrees of freedom for node I in the x and y directions are respectively denoted by $\mathbf{u}_{Ix}$ and $\mathbf{u}_{Iy}$, as shown below.

$$\boldsymbol{\psi}_I^{1,2} = \begin{bmatrix} \psi_{I(0,0)} & \psi_{I(1,0)}^{C_x} & \dots & \psi_{I(n,m)}^{S-} \end{bmatrix} \tag{14}$$

$$\boldsymbol{u}_{Ix}^{\top} = [u_{Ix(0,0)}, u_{Ix(1,0)}^{C_x}, ..., u_{Ix(n,m)}^{S-}] \tag{15}$$

$$\boldsymbol{u}_{Iy}^{\top} = [u_{Iy(0,0)}, u_{Iy(1,0)}^{C_x}, ..., u_{Iy(n,m)}^{S-}] \tag{16}$$

In the above formulation $\psi_{I(0,0)} = N_I$ denote regular Lagrangian interpolation functions and $\psi_{I(k_x,k_y)}^{\gamma} = N_I\phi_{(k_x,k_y)}^{\gamma}$ are the GFEM interpolation functions in which $\phi_{(k_x,k_y)}^{\gamma}$ with the corresponding superscript denotes the following trigonometric basis functions:

$$\phi_{(k_x,0)}^{C_x} = cos(\frac{2\pi k_x x}{\Lambda_x}), \quad \phi_{(k_x,0)}^{S_x} = sin(\frac{2\pi k_x x}{\Lambda_x}),$$

$$\phi_{(0,k_y)}^{C_y} = cos(\frac{2\pi k_y y}{\Lambda_y}), \quad \phi_{(0,k_y)}^{S_y} = sin(\frac{2\pi k_y y}{\Lambda_y})$$

$$\phi_{(k_x,k_y)}^{C+} = cos(\frac{2\pi k_x x}{\Lambda_x} + \frac{2\pi k_y y}{\Lambda_y}), \quad \phi_{(k_x,k_y)}^{S+} = sin(\frac{2\pi k_x x}{\Lambda_x} + \frac{2\pi k_y y}{\Lambda_y})$$

$$\phi^{C-}_{(k_x,k_y)} = cos(\frac{2\pi k_x x}{\Lambda_x} - \frac{2\pi k_y y}{\Lambda_y}), \quad \phi^{S-}_{(k_x,k_y)} = sin(\frac{2\pi k_x x}{\Lambda_x} - \frac{2\pi k_y y}{\Lambda_y})$$

where k_x and k_y are the wave numbers varying from 1 to n and 1 to m, respectively. n and m are the integer cutoff numbers for enrichments in x and y directions, respectively.

3.1.2. Pore pressure field discretization

Following the general idea of the PNM-GFEM, in the case of impervious crack faces (i.e., discontinuous pore pressure field), the pore pressure approximation in fractured elements is

$$p(x,y,t) = H(-f(x,y)) \sum_{I\in S_1} \left(\boldsymbol{\psi}^3_I(x,y)\boldsymbol{p}_I(t)\right) + H(f(x,y)) \sum_{I\in S_2} \left(\boldsymbol{\psi}^3_I(x,y)\boldsymbol{p}_I(t)\right) \tag{17}$$

in which $\boldsymbol{\psi}^3_I$ denotes the set of conventional and enriched interpolation functions for the pore pressure variable, and $\boldsymbol{p}_I$ is the vector of corresponding regular and enriched, phantom or real pore pressure degrees of freedom for node I.

$$\boldsymbol{\psi}^3_I = \left[\begin{array}{cccc} \psi_{I(0,0)} & \psi^{C_x}_{I(1,0)} & \ldots & \psi^{S-}_{I(n,m)} \end{array} \right] \tag{18}$$

3.2. Discretized mixed finite element equations

Semi-discretized system of equations can be developed by substitution of the specified displacement interpolation functions (12)- (13) and pore pressure field (17) in the weak form (10)-(11):

$$\sum_{J=1}^{n_{node}} \left([M^e]^{11}_{IJ}\ddot{\mathbf{u}}^e_{Jx} + [K^e]^{11}_{IJ}\mathbf{u}^e_{Jx} + [K^e]^{12}_{IJ}\mathbf{u}^e_{Jy} + [K^e]^{13}_{IJ}\mathbf{p}^e_J\right) = \mathbf{F}^e_{Iu_x}, \quad (I = 1, ..., n_{node}) \tag{19}$$

$$\sum_{J=1}^{n_{node}} \left([M^e]^{22}_{IJ}\ddot{\mathbf{u}}^e_{Jy} + [K^e]^{21}_{IJ}\mathbf{u}^e_{Jx} + [K^e]^{22}_{IJ}\mathbf{u}^e_{Jy} + [K^e]^{23}_{IJ}\mathbf{p}^e_J\right) = \mathbf{F}^e_{Iu_y}, \quad (I = 1, ..., n_{node}) \tag{20}$$

$$\sum_{J=1}^{n_{node}} \Big([M^e]^{31}_{IJ}\ddot{\mathbf{u}}^e_{Jx} + [M^e]^{32}_{IJ}\ddot{\mathbf{u}}^e_{Jy} + [C^e]^{31}_{IJ}\dot{\mathbf{u}}^e_{Jx} + [C^e]^{32}_{IJ}\dot{\mathbf{u}}^e_{Jy} +$$

$$[C^e]^{33}_{IJ}\dot{\mathbf{p}}^e_J + [K^e]^{33}_{IJ}\mathbf{p}^e_J\Big) = \mathbf{F}^e_{Ip}, \quad (I = 1, ..., n_{node}) \tag{21}$$

in which n_{node} is the number of nodes in each of the two superposed elements 1 and 2, and includes both original real and fictitious/phantom nodes. In an element crossed by a crack, the definitions of $[M^e]_{IJ}$, $[C^e]_{IJ}$, $[K^e]_{IJ}$, $\mathbf{F}^e_{Iu_x}$, $\mathbf{F}^e_{Iu_y}$, and $\mathbf{F}^e_{Ip}$ in (19), (20), and (21) for each of the superimposed elements, i.e., e= 1 or 2, are given in the Appendix.

The semi-discretized coupled hydro-mechanical poro-elastic finite element equations (19), (20), and (21) can be rewritten in a more compact form as:

$$[M]\left\{\ddot{\mathbf{\Delta}}\right\} + [C]\left\{\dot{\mathbf{\Delta}}\right\} + [K]\{\mathbf{\Delta}\} = \{\mathbf{F}\} \tag{22}$$

where $\{\mathbf{\Delta}\} = \{\mathbf{u}_x \;\; \mathbf{u}_y \;\; \mathbf{p}\}^\top$ is the vector of unknown nodal values for displacement and pore pressure degrees of freedom in the porous media, and $\{\mathbf{F}\} = \left\{\mathbf{F}_{u_x} \;\; \mathbf{F}_{u_y} \;\; \mathbf{F}_p\right\}^\top$ is the vector of mechanical forces and flow fluxes.

The G22 and G11 generalized Newmark implicit schemes are employed for time integration of displacement and pore pressure degrees of freedom, respectively. To this end, the values of the first- and second-order time derivatives of the variables at time step $(i+1)$ are represented in terms of the corresponding values of the variables at the current time step (i) and unknown values of the variables at time step $(i+1)$ through the following relationships:

$$\dot{p}_{i+1} = \frac{1}{\theta\Delta t}(p_{i+1} - p_i) - (\frac{1}{\theta} - 1)\dot{p}_i \tag{23}$$

$$\dot{u}_{i+1} = \frac{\gamma}{\beta\Delta t}(u_{i+1} - u_i) - (\frac{\gamma}{\beta} - 1)\dot{u}_i - \Delta t(\frac{\gamma}{2\beta} - 1)\ddot{u}_i \tag{24}$$

$$\ddot{u}_{i+1} = \frac{1}{\beta\Delta t^2}(u_{i+1} - u_i) - \frac{1}{\beta\Delta t}\dot{u}_i - (\frac{1}{2\beta} - 1)\ddot{u}_i \tag{25}$$

where γ, β, and θ are the integration parameters that are set to be 0.7 in the numerical examples of the present work to preserve the unconditional stability condition of the time integration [41]. However, due to the transient nature of wave propagation, sufficiently small time steps need to be considered to obtain converged results.

4. Interface simulation

Geomechanical formations experience huge amounts of overburden and horizontal in-situ stresses leading to significant normal and frictional contact forces acting along natural and induced fractures and faults. In the context of the partition-of-unity finite element a noticeable amount of research has been dedicated to the imposition of inter-facial constraints [38, 39, 40, 41]. In this work, a stable augmented Lagrange multiplier approach is adopted to enforce the frictional contact via an iterative method.

Accounting for the contact force contributions, the weak form (10) is transformed as:

$$\int_{\Omega} \boldsymbol{\sigma} : \delta\boldsymbol{\varepsilon}\ d\Omega + \int_{\Omega} \rho\ddot{\boldsymbol{u}} \cdot \delta\boldsymbol{u}\ d\Omega - \int_{\Gamma_t} \bar{\boldsymbol{t}} \cdot \delta\boldsymbol{u}\ d\Gamma - \int_{\Omega} \rho\boldsymbol{b} \cdot \delta\boldsymbol{u}\ d\Omega - \int_{\Gamma_d} \bar{\lambda}_N g_N d\Gamma - \int_{\Gamma_d} \bar{\lambda}_T g_T d\Gamma = 0 \tag{26}$$

Normal contact traction, normal inter-penetration, tangential contact frictional traction, and tangential slip across the interface are denoted by $\bar{\lambda}_N$, g_N, $\bar{\lambda}_T$, and g_T , respectively.

One-dimensional elements are used along the interface to interpolate the contact force/Lagrange multiplier fields:

$$\bar{\lambda}_N = \tilde{\mathbf{N}}\bar{\boldsymbol{\lambda}}_N \text{ and } \bar{\lambda}_T = \tilde{\mathbf{N}}\bar{\boldsymbol{\lambda}}_T \tag{27}$$

Here, $\tilde{\mathbf{N}}$ denotes linear one-dimensional Lagrangian shape functions, and $\left(\bar{\boldsymbol{\lambda}}_N, \bar{\boldsymbol{\lambda}}_T\right)$ are the vectors of Lagrange multiplier degrees of freedom for normal and friction contact forces. To ensure the stability of the interface contact solution, the nodes of the Lagrange multiplier mesh are chosen using the Vital Vertex Method [39, 40].

At each time step, $\boldsymbol{\Delta}_{n+1}$ and $\left(\bar{\boldsymbol{\lambda}}_N, \bar{\boldsymbol{\lambda}}_T\right)_{n+1}$ are sought using an iterative procedure. The iterative process starts ($k = 0$) with an initial guess for the vector of Lagrange multipliers $\left(\bar{\boldsymbol{\lambda}}_N, \bar{\boldsymbol{\lambda}}_T\right)_{n+1}^{k=0} = \left(\bar{\boldsymbol{\lambda}}_N, \bar{\boldsymbol{\lambda}}_T\right)_n$. Given $\left(\bar{\boldsymbol{\lambda}}_N, \bar{\boldsymbol{\lambda}}_T\right)_{n+1}^{k}$ at iteration k, the linear fully-discretized system of equations is solved for $\boldsymbol{\Delta}_{n+1}^{k}$, from which the normal interpenetration g_N^k and tangential slip g_T^k of the crack at each node of the Lagrange multiplier mesh are calculated. The Lagrange multiplier nodal vectors are updated if the gap norms surpass a defined tolerance. In the case of frictional contact, interface slippage occurs, $g_T > 0$, if the tangential frictional contact force, $\bar{\lambda}_T$, required to prevent slip exceeds the limit $\bar{\lambda}_T^{max} = \bar{\lambda}_N \mu_f$ (μ_f is the friction coefficient). Otherwise the interface is in the stick state.

5. Results and discussion

In this section, the simulation of acoustic wave emission due to sudden release of strain energy (in shear mode) at interface location is carried out. The domain of analysis is assumed to be a two-dimensional isotropic-homogeneous poroelastic media with hydro-mechanical properties given in Table 1, unless stated

Table 1: Material properties of the porous media.

$E(Pa)$	ν	$\rho_s(kg/m^3)$	$\rho_f(kg/m^3)$	n'	$k_f(m^3s/kg)$	$K_f(Pa)$	$K_s(Pa)$
14.516×10^6	0.3	2000	1000	0.3	1.0194×10^{-6}	2.1×10^9	1×10^{20}

otherwise. Based on the magnitudes considered for the bulk moduli of solid skeleton and pore fluid, the material is compressible. It is worth mentioning that the numerical model developed in this paper is a general computational scheme for simulation of acoustic emissions induced by shear slip on material interfaces and can be employed for different types of materials with different inhomogeneity and anisotropy conditions and randomness in material and geometry characteristics (e.g., randomly distributed cracks). A unit thickness is assumed in the out-of-plane direction. It is noted that proportional damping in the form of $\mu_1[M] + \mu_2[K]$ is assumed to describe the physical attenuation of waves in the solid phase of the media, in which μ_1 and μ_2 are the damping coefficients corresponding to the mass and stiffness matrices of the solid phase, respectively. It is important to mention that, to the best of the authors' knowledge there is no analytic models in the literature on acoustic emissions induced by shear failure under frictional contact condition. However, a study is carried out below showing that the AE wave forms obtained using the developed computational model with frictional contact at interface converge with mesh refinement. It is also noted that the numerical method in this work (i.e., PNM-GFEM) has been well-established in a couple of recent papers (see [30, 42]).

5.1. Acoustic emission simulation due to shear failure of an interface

5.1.1. Simulation of acoustic signal

To have a better intuition about how local release of strain energy can trigger acoustic emission in a medium, a two-dimensional domain of $1m$ by $0.5m$ is considered. A sloping crack of length $0.36m$ orientated at the angle $\theta = 56^0$ with respect to the horizontal direction is embedded in the medium and frictional contact state is considered at the interface. The friction coefficient is assumed to be $\mu_f = 0.6$ along the embedded interface. The domain is discretized using 30×10 rectangular elements. The porous medium is subjected to a bilateral confining stress, imposed by compressive tractions of $\bar{t} = 10kN/m^2$ acting of the left and top edges of the domain.

The geometry of the medium and the fracture, boundary conditions and the imposed loads are shown in Figure 2. All the edges are assumed to be hydraulically drained. The simulation starts by the release of the friction/tangential contact constraint at the interface to induce an acoustic response through the release of energy stored in the system due to the initial in-situ stresses. Damping coefficients of the solid phase are assumed to be $\mu_1 = 0.01, \mu_2 = 0.01$. The time steps size for the implicit time integration scheme is

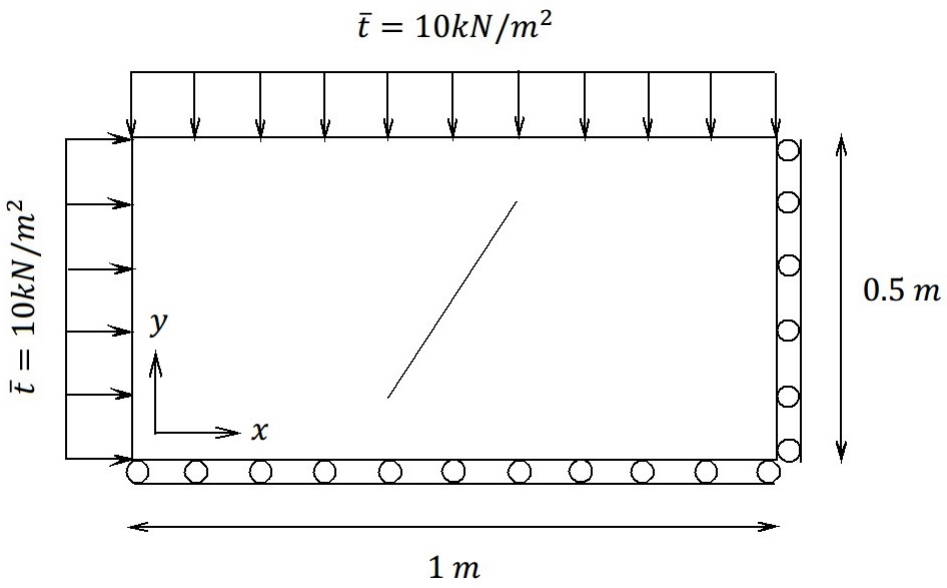

Figure 2: A schematic figure of fractured porous media of section 5.1.

$\Delta T = 2 \times 10^{-4} s$. To investigate the dynamic response of the system, time histories of the problem variables at point $(x = 0.9667, y = 0.25)$ are recorded. Figure 3 shows the x-velocity signal due to the release of friction at the interface using regular PNM and enriched PNM-GFEM. The enriched model gives a more oscillation-free acoustic signal. As seen in Figure 3b, the non-physical oscillations that appear in regular PNM simulation of the velocity signal are effectively inhibited using the enriched model (i.e., PNM-GFEM-M model).

The pore pressure time signal of the acoustic emission is shown in Figure 4 for regular and enriched finite element simulations. It is clear in this figure that using the enriched FE model results in acoustic data which is free of high-frequency oscillations at the signal's peak.

Figure 5 illustrates the effect of damping coefficients on the acoustic response of the system. The results are obtained by changing the damping coefficients of the solid phase. Enriched models are used with $(n = 1)$. As seen in this figure, the high-frequency components of the signal are dissipated very quickly by increasing the physical damping of the solid skeleton.

To have a better understanding about the spectral/frequency contents, a Fast Fourier Transform (FFT) is employed to acquire the frequency spectrum of the signal, as shown in Figure 6. The high-frequency components of the signal are dissipated by increasing the damping coefficients. However, unlike the magnitude spectrum, the peak frequencies of the spectrum (i.e., frequencies associated with peak magnitudes) do not

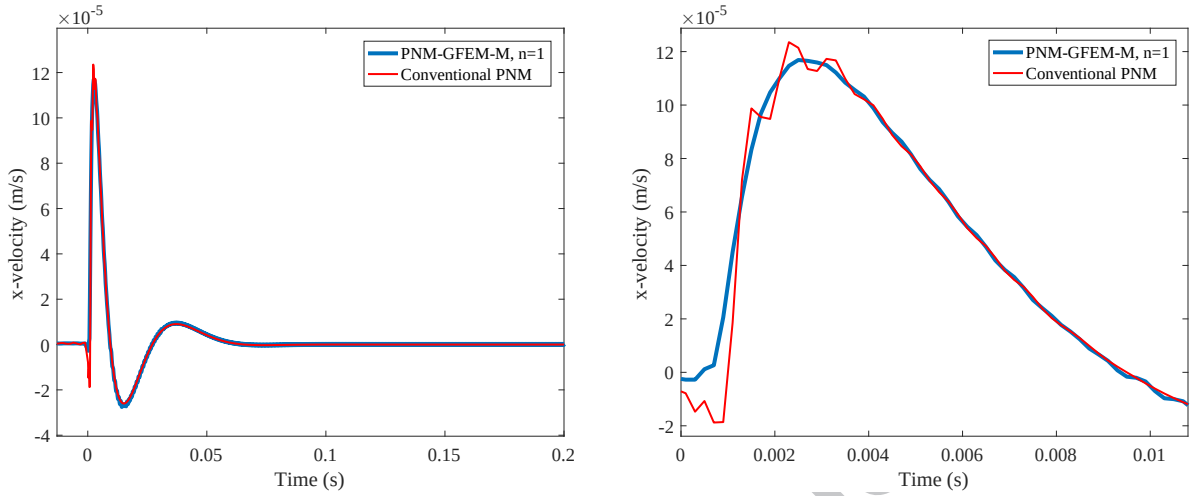

Figure 3: Time history of x-velocity at point $(x = 0.9667, y = 0.25)$ using regular and enriched PNM models.

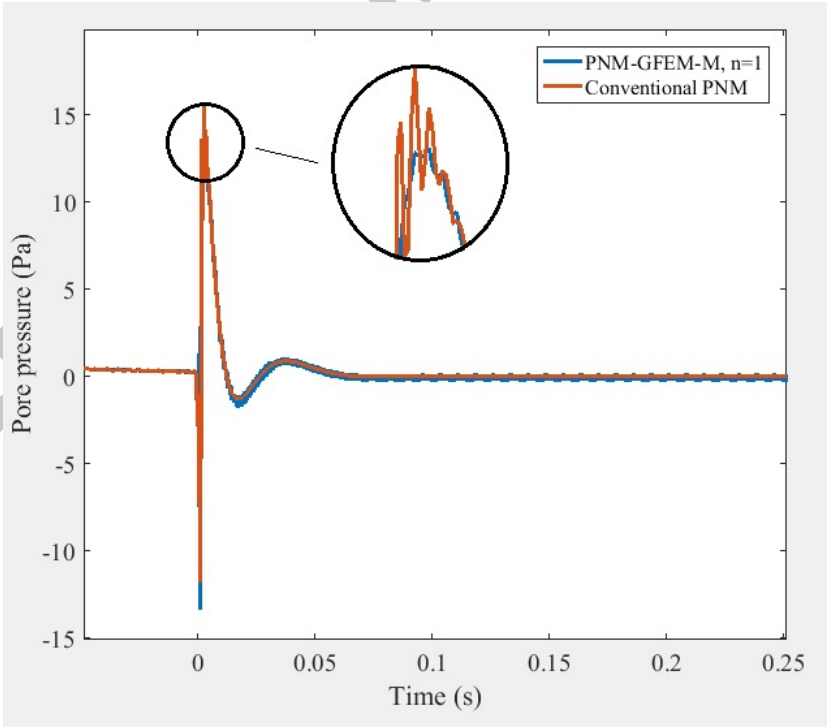

Figure 4: Time history of pore pressure signal at point $(x = 0.9667, y = 0.25)$ using regular and enriched models.

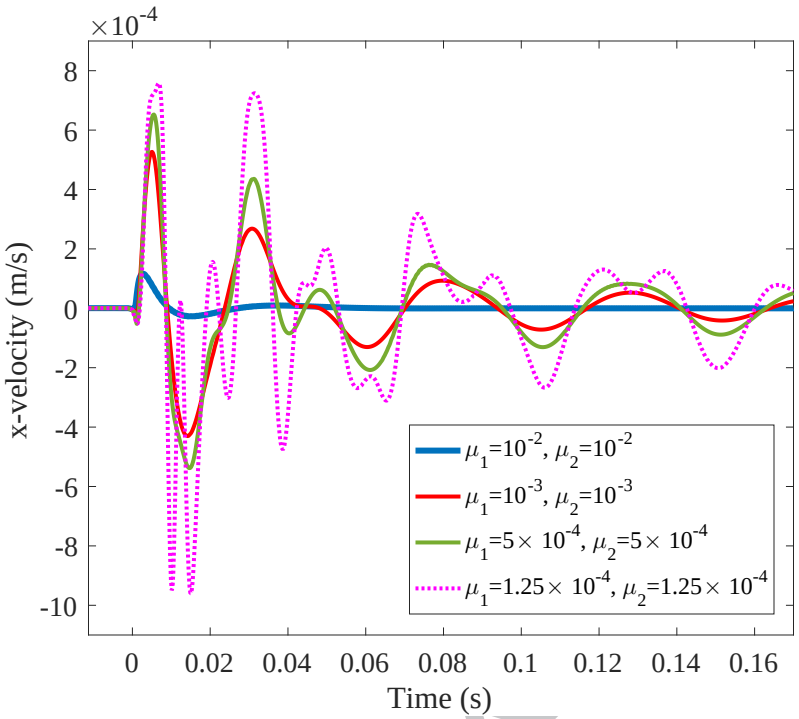

Figure 5: Effect of the damping values on the time history of acoustic signal at point $(x = 0.9667, y = 0.25)$.

seem to be significantly affected by the damping magnitudes of the solid skeleton.

Effect of permeability on the acoustic signal

To assess the effect of the permeability of porous media on acoustic response, the case study shown schematically in Figure 2 is considered. Figures 7 and 8a show, respectively, plots of x-displacement and x-velocity versus time at point $(x = 0.9667, y = 0.25)$ for various values of permeability. As seen in these figures, the lower the permeability the smaller the peak amplitudes of the acoustic signal. This behaviour can be attributed to the inversely proportional correlation between permeability and viscous damping in porous media which results in more energy dissipation in low-permeability materials. Also, as seen in the figures, the dynamic behaviour of lowest permeable domain cases exhibits the highest frequencies in the induced signal. This can be explained by the fact that the behaviour of the lower permeable domain is more undrained. Figure 8b gives a close-up of the time history presented in Figure 8a. By decreasing the amount of permeability (i.e., getting close to material incompressibility condition) the time signal (mixed finite element solutions in general) gets more vulnerable to numerical dispersions and prone to showing spurious oscillations. As observed in Figure 8b, the non-physical oscillations that are stimulated in regular finite element simulation of the low-permeable case can be eliminated through the enriched finite element

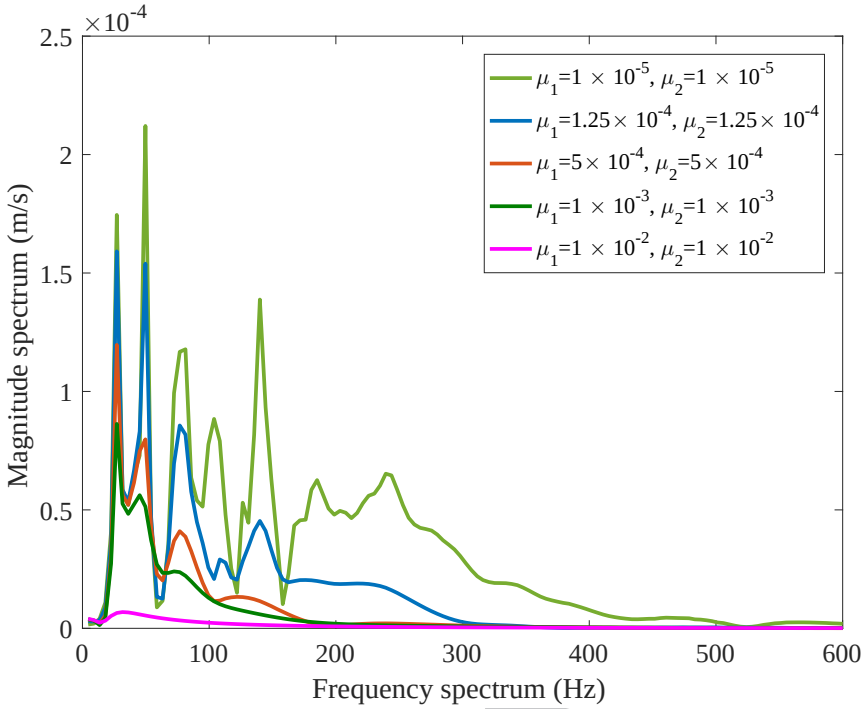

Figure 6: Frequency domain response of the acoustic signal of figure 5.

model (i.e., PNM-GEFM-M) with ($n = 1$).

5.1.2. Acoustic wave pattern

To visualize the pattern of an acoustic wave propagation under shear failure, a porous domain of size $3m \times 3m$ is considered. A single fracture is embedded at the center of the domain which is $0.1m$ in length and is orientated at the angle of 45^o with respect to the horizontal direction. The friction coefficient of the interface is assumed to be $\mu_f = 0.6$ and the damping coefficients of the solid phase are $\mu_1 = \mu_2 = 0.001$. Confining tractions of $\bar{t} = 10kN/m^2$ and $\bar{t} = 5kN/m^2$ are imposed at the left and top surfaces, respectively. The domain is discretized using 90×90 rectangular elements. Simulation starts at $t = 0.0s$ by releasing the friction condition at the interface. Figure 9 demonstrates consecutive snapshots of x-velocity contours at some time steps. Transient propagation pattern of the acoustic wave emission due to the induced abrupt slip at the interface (which is followed by a sudden release of accumulated-strain-energy) is transparent in the figures.

To have a better visual intuition about the wave propagation pattern, Figure 10 shows the absolute velocity (i.e., $\sqrt{(\dot{u}_x)^2 + (\dot{u}_y)^2}$) contours of the same problem at several time steps after the acoustic emission is triggered, using a 180×180 mesh resolution. Symmetric pattern of the wave propagation with respect to the shear failure (fracture) direction is apparent in the snapshots. Due to the attenuation of the porous

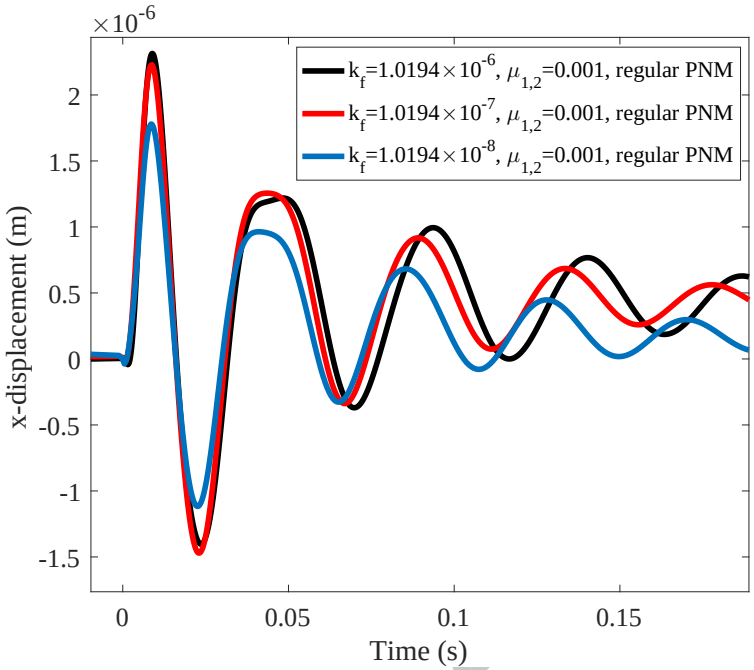

Figure 7: Time history of x-displacement for various values of permeability.

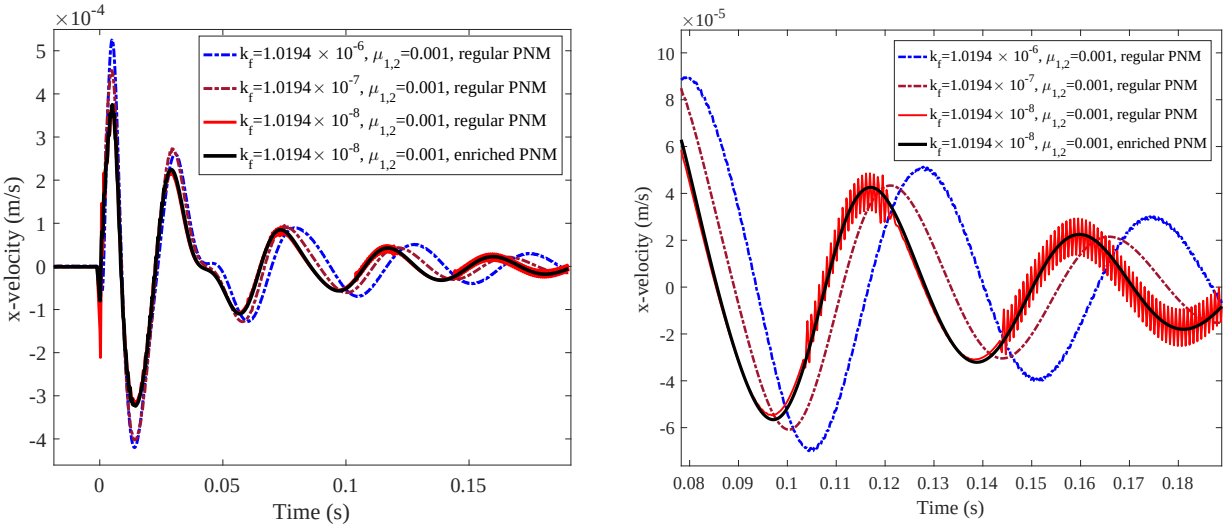

(a) (b)

Figure 8: Time history of x-velocity acoustic signal for various values of permeability.

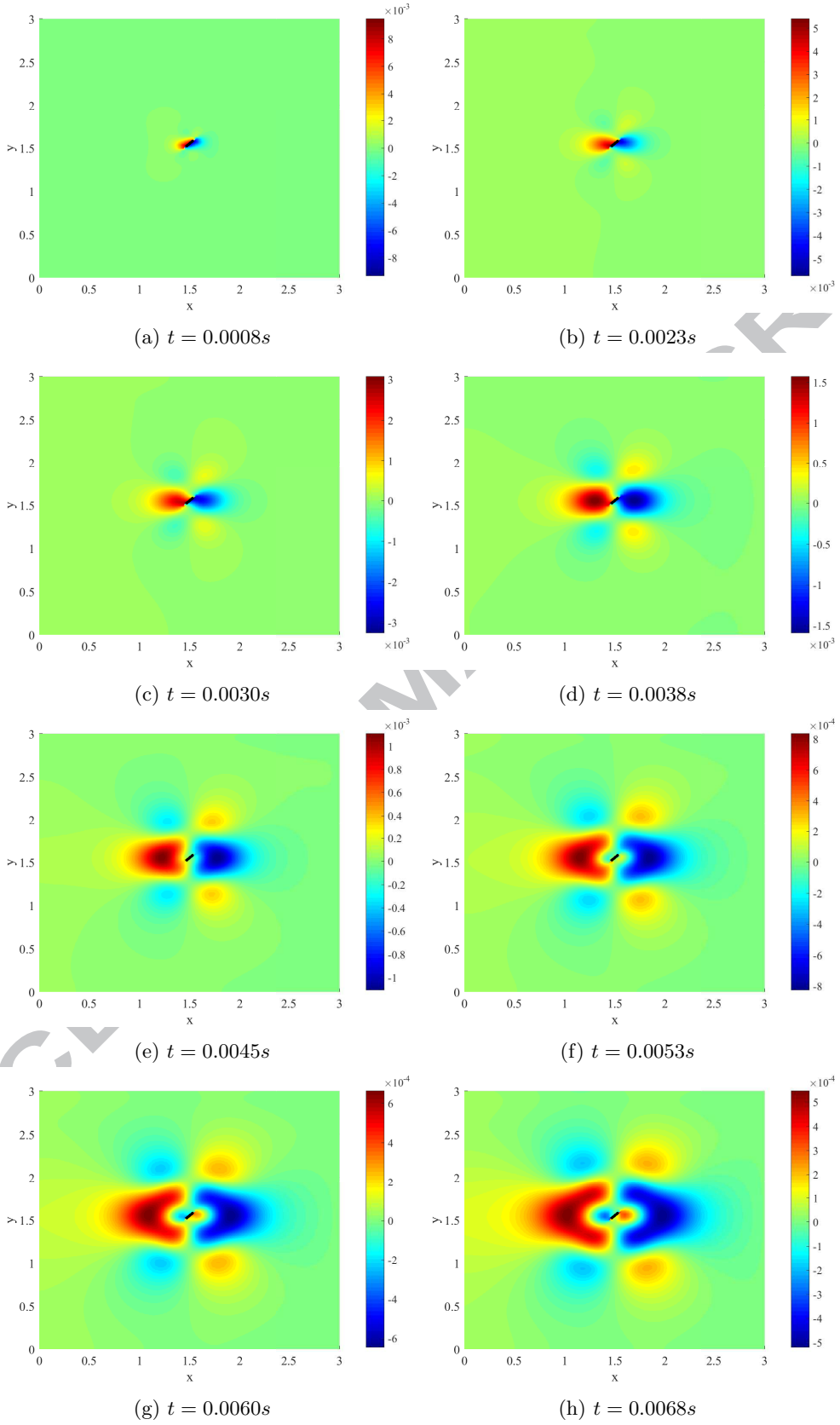

(a) $t = 0.0008s$ (b) $t = 0.0023s$

(c) $t = 0.0030s$ (d) $t = 0.0038s$

(e) $t = 0.0045s$ (f) $t = 0.0053s$

(g) $t = 0.0060s$ (h) $t = 0.0068s$

Figure 9: x-velocity contour of acoustic wave propagation under shear failure.

media (in both phases), the velocity magnitude decays as the wave travels in the medium. Figure 11 shows the wave pattern at time $t = 0.0047s$ in a three-dimensional perspective from a different (angled) view.

Role of material damping

To investigate the effect of material viscous damping on the microseismic response in porous media, Figure 12 illustrates acoustic wave propagation pattern in a $6m \times 6m$ domain with a fracture of length $0.2m$ located at the center of the domain and with an orientation of 45^o from the horizontal direction. Confining tractions of $\bar{t} = 10kN/m^2$ and $\bar{t} = 5kN/m^2$ are applied at the left and top surfaces, respectively. In this case, lower damping coefficients ($\mu_1 = \mu_2 = 0.00005$) are considered for the analysis compared to those assumed in the previous example. Comparing the results obtained for $\mu_1 = \mu_2 = 0.001$ in Figure 10 and $\mu_1 = \mu_2 = 0.00005$ in Figure 12 shows that in the case with higher viscous damping the wave contours are overly-diffusive with very smoothly varying front. Unlike the case with high attenuation, the wave impulse in the low viscosity domain has a highly-transient pattern with a sharp wave front due to the high-frequency components of the dynamic response. It is noted that the high-frequency contents get dissipated by increasing the physical damping of the system which contributes to more diffusive wave patterns and results in losing the highly-transient behaviour and the sharp wave front.

Microseismic emission from multiple cracks and coalescence of waves

We consider the domain that was assumed in the previous example with the same loading condition and characteristics. In this case two identical sloping cracks (with the same length and direction as the previous example) are embedded in the medium as shown in Figure 13. The process of concurrent acoustic emissions from the fractures, and interaction of the emitted waves are illustrated in Figure 13 through snapshots of the velocity contours in some time steps.

To show the versatility of the method in modeling multiple randomly-distributed cracks, Figure 14 illustrates the AE patterns induced by shear slip on three discontinuities at $t = 0.005s$. The same in-situ stress and boundary conditions as the previous example are considered. The poroelastic domain is assumed to be $3m \times 3m$.

Discretization sensitivity

In this part the sensitivity of the discretization of the developed model in the simulation of induced AEs is assessed. To this end, a porous media of size $3m \times 3m$ is considered with a single fracture of length $0.2m$ located in the center of the domain and oriented at the angle of 45^o with respect to the horizontal direction. The same in-situ stresses, boundary conditions, and material properties as the previous example are assumed.

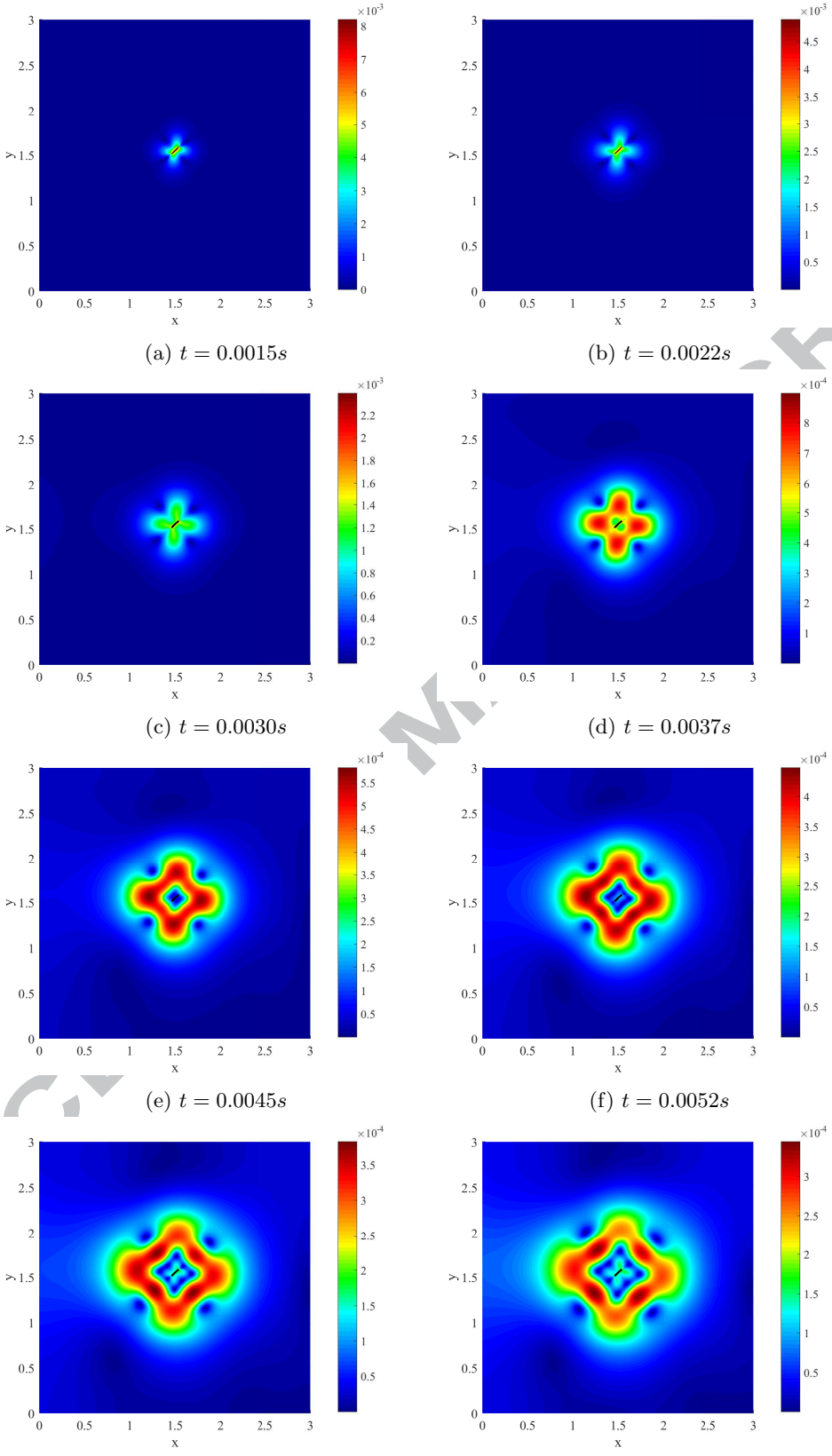

(a) $t = 0.0015s$ (b) $t = 0.0022s$

(c) $t = 0.0030s$ (d) $t = 0.0037s$

(e) $t = 0.0045s$ (f) $t = 0.0052s$

(g) $t = 0.0060s$ (h) $t = 0.0067s$

Figure 10: Absolute velocity contours of acoustic wave propagation under shear failure with viscous damping coefficients $\mu_1 = \mu_2 = 0.001$.

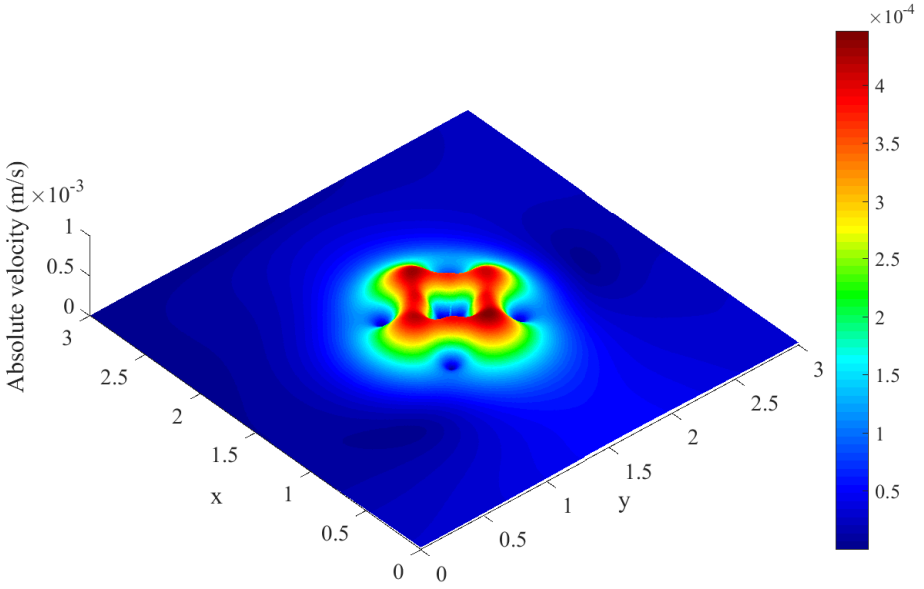

Figure 11: Absolute velocity wave pattern of acoustic emission at $t = 0.0047s$.

Figure 15 illustrates AE wave patterns at $t = 0.01s$ for different meshes. As seen, the amplitude of the wave pulse converges with mesh refinement.

5.2. Acoustic emission due to injection-induced slip instability

A $1m$ by $0.5m$ porous medium discretized by 30×10 rectangular elements is considered. The domain is assumed to be under the effect of a bilateral confining tractions of $2kN/m^2$ on the left and top edges. A $0.36m$ long inclined crack is embedded at the angle of $\theta = 56^0$ with respect to the horizontal direction. The friction coefficient is assumed to be $\mu_f = 0.8$. Damping coefficients of the solid skeleton are considered as $\mu_1 = 0.1, \mu_2 = 0.1$. The domain, the fracture, and applied loads are depicted in Figure 16. A PNM-GFEM-M model with $n = 1$ is used with time step size of $\Delta t = 1$ms.

The simulation commences by applying a constant fluid flux injection of $q = 0.1m^3/s$ at the center of the domain at $t = 0.0s$. Prior to applying the injection, strain energy is stored in the system due to the initial stress caused by confining tractions and the frictional contact at the interface of the fracture.

Due to injection of the fluid, a sudden slip between fracture faces occurs along the interface. This abrupt transition from a stick condition to a slip situation induces an AE response- the rapid release of strain energy results in the stimulation of inertia effects. Figure 17 depicts the acoustic signal at point $(x = 0.9667, y = 0.25)$ induced by the injection perturbation. As seen in this figure, in the case in which there is no frictional resistance/contact at the fracture interface (i.e., when $\mu_f = 0.0$), no acoustic behaviour is observed in the dynamic response of the system, which is quite rational and expected. In the case of

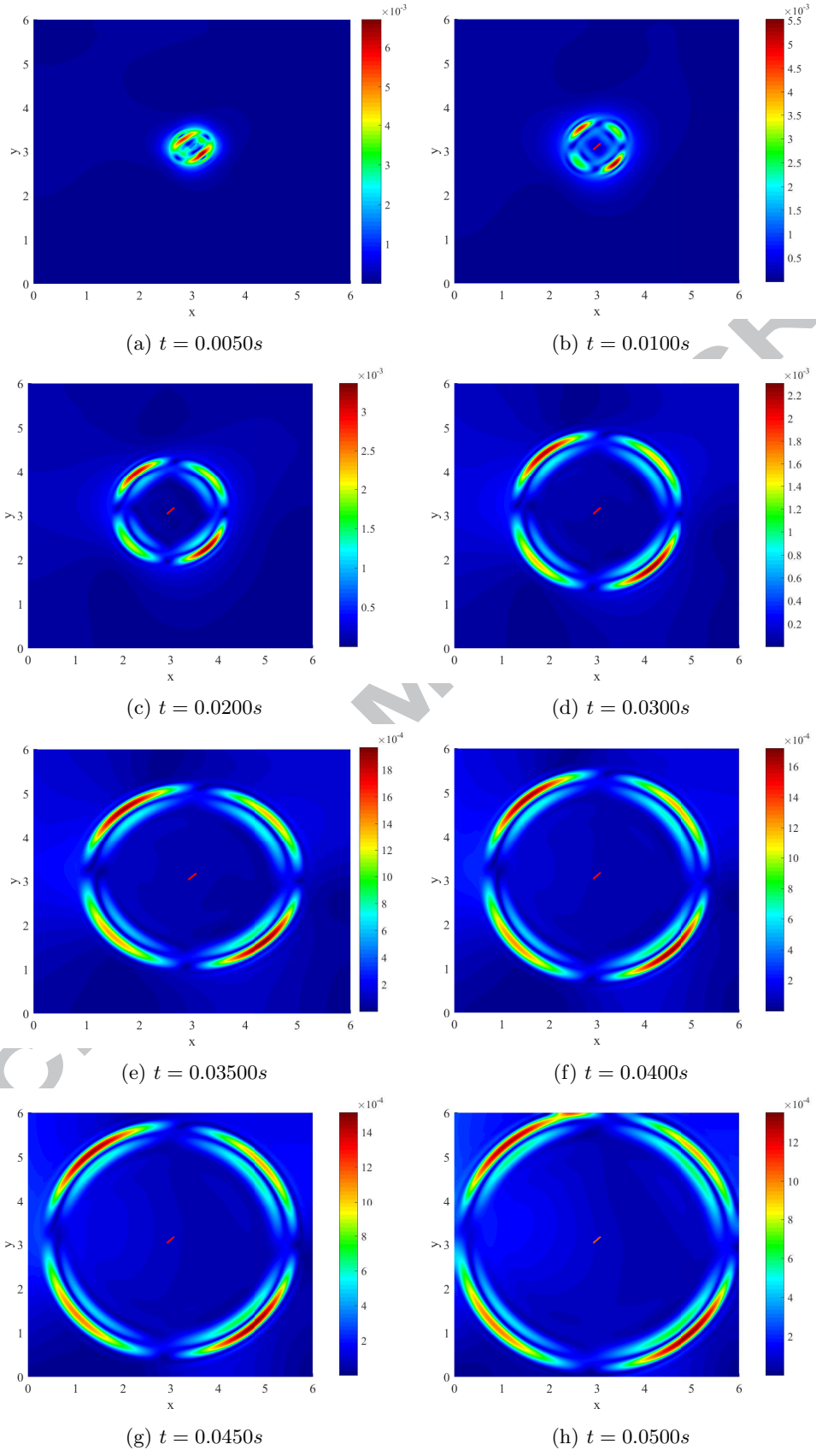

(a) $t = 0.0050s$ (b) $t = 0.0100s$

(c) $t = 0.0200s$ (d) $t = 0.0300s$

(e) $t = 0.03500s$ (f) $t = 0.0400s$

(g) $t = 0.0450s$ (h) $t = 0.0500s$

Figure 12: Absolute velocity contours of acoustic wave propagation under shear failure with viscous damping coefficients $\mu_1 = \mu_2 = 0.00005$.

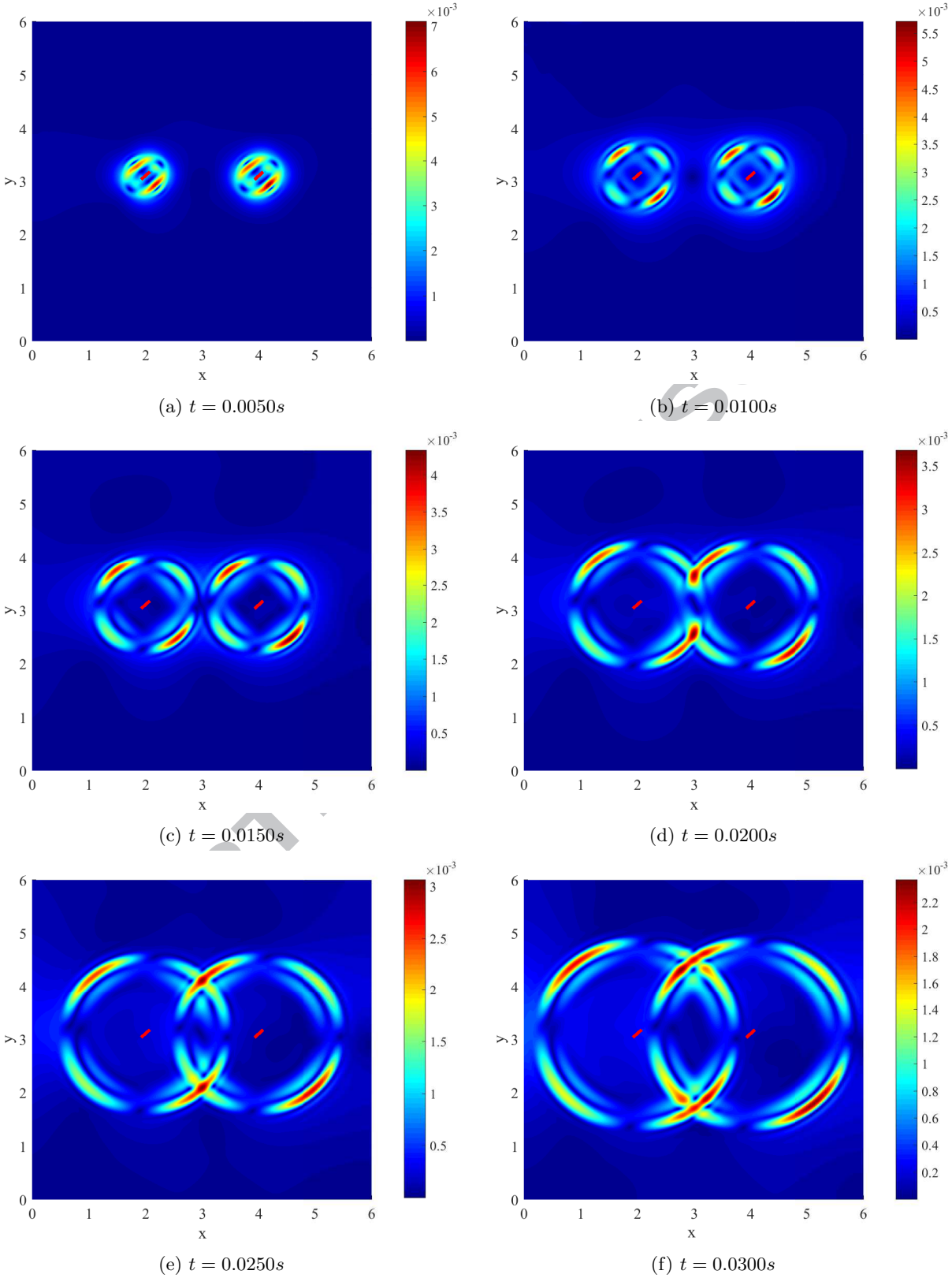

(a) $t = 0.0050s$

(b) $t = 0.0100s$

(c) $t = 0.0150s$

(d) $t = 0.0200s$

(e) $t = 0.0250s$

(f) $t = 0.0300s$

Figure 13: Absolute velocity contours of acoustic wave propagation due to double shear failures and interaction of emitted waves.

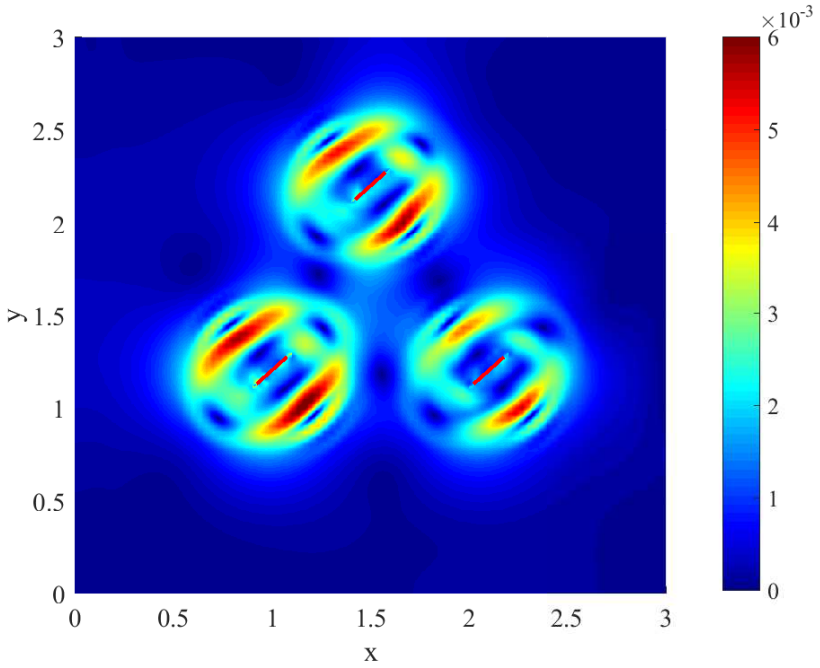

Figure 14: Absolute velocity contour of AE wave pattern induced by shear slip instability of multiple randomly-distributed fractures at $t = 0.005s$.

$\mu_f = 0$ (no friction and therefore no stick condition under the in-situ stresses), unlike the frictional contact case, there is no sudden transition from a stick to a slip state. This is why no acoustic response is seen in the case of frictionless interface.

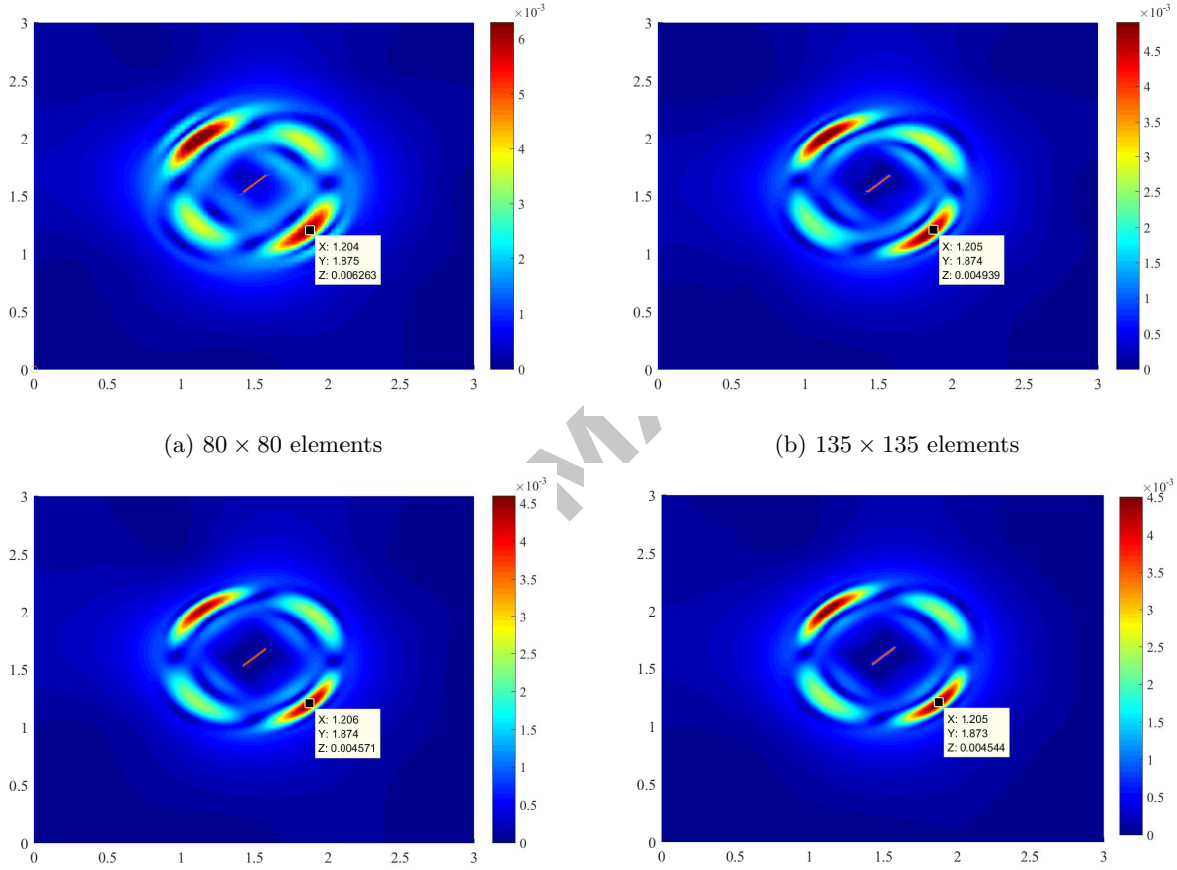

(a) 80 × 80 elements

(b) 135 × 135 elements

(c) 180 × 180 elements

(d) 200 × 200 elements

Figure 15: Mesh-sensitivity study of an AE wave pattern obtained using the enriched model with $n = m = 1$.

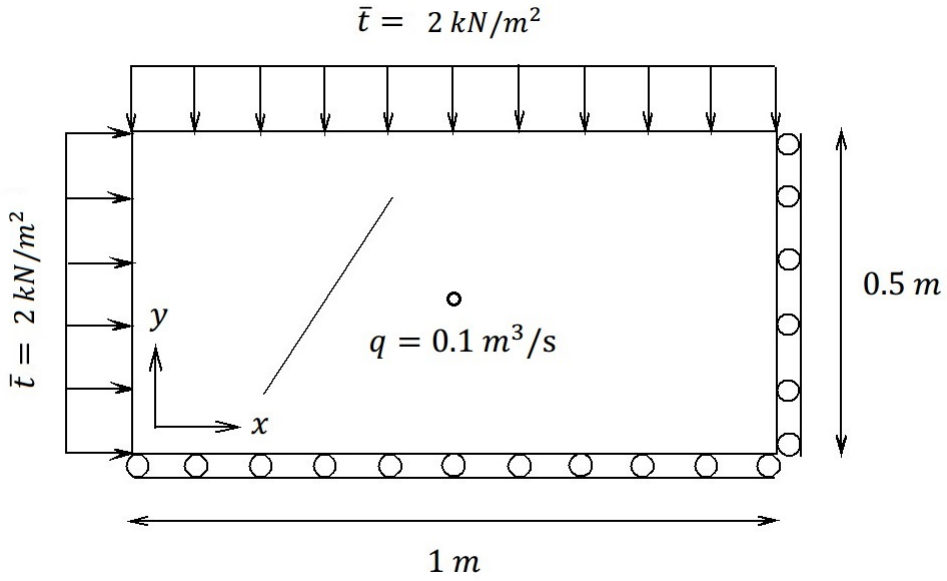

Figure 16: A schematic figure of fractured porous media under confining tractions and point injection at the middle, considered in section 5.2.

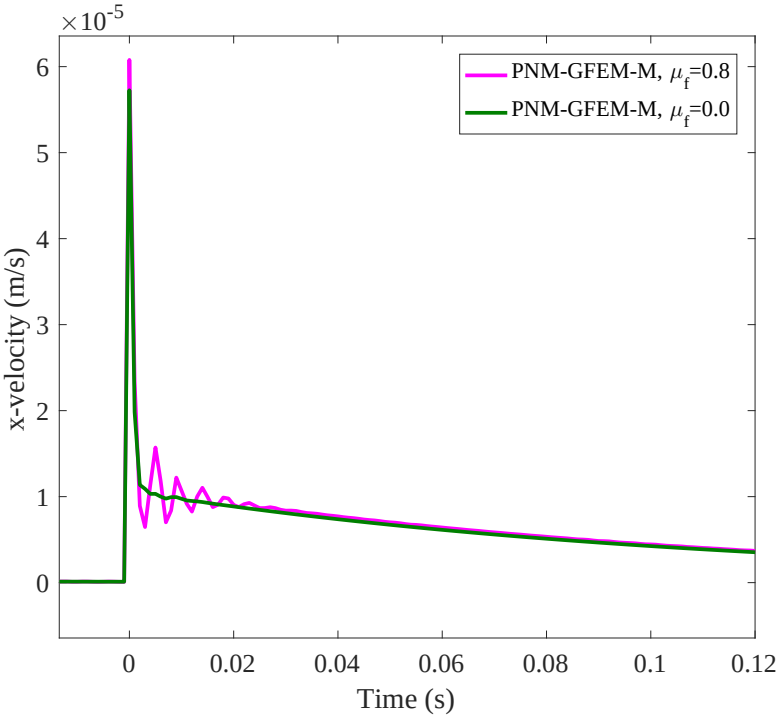

Figure 17: Acoustic signal at point $(x = 0.9667, y = 0.25)$, induced due to a sharp switch from stick to slip condition at the fracture interface under injection.

6. Conclusion

Acoustic emission (AE) induced by shear failure and slip along fractures in porous media is simulated and the role of permeability, interface friction and other system characteristics on the AE are studied. To model interface (e.g., fracture or fault) in continua, Phantom Node Method (PNM) is used in conjunction with global Generalized Finite Element Method (GFEM) harmonic enrichment functions to solve dynamic/wave propagation problem. A seismic emission is triggered by the sudden release of strain energy, which occurs due to an abrupt switch from a stick to a slip condition (localization) in the form of interface snap-through instability/bifurcation. The required perturbation for instability stimulation at the interface is provided through an external excitation such as fluid injection in the vicinity of the fracture under confining stresses and frictional contact conditions.

Effects of hydro-mechanical characteristics such as viscous damping parameters of the solid phase, permeability of porous media, and interface friction on AE are assessed based on the numerical simulations performed using the proposed computational model. It should be noted that there was no available data in the literature to use for conducting comparison studies on shear slip-induced AE results of this work. Therefore, further research studies (numerical and experimental) should be carried out as scientific supports for the conclusions of this paper. Based upon the simulation results of the method introduced in this paper, it is found that the acoustic response in lower permeability cases shows higher frequency and lower amplitude signals. Increasing the damping magnitude significantly affects the spectral contents of the acoustic signal by attenuating the high-frequency components and decreasing the corresponding magnitudes. By increasing damping, the acoustic emission pattern changes from the state of very transient wave propagation to overly-diffusive (diffusion-dominated) response. Also, it is shown that the magnitude of induced acoustic signal is directly dependent on the friction coefficient at the interface. The superiority of the enriched mixed finite element model in simulation of acoustic waves and suppressing the spurious oscillations in pore pressure and velocity time signals that appear in acoustic simulations using regular finite element approach is also demonstrated.

As shown throughout the article, the proposed PNM-GFEM-M numerical model is a very promising computational approach for simulation of localization-induced acoustic/seismic waves in fractured porous media. However, many items need to be tackled in future studies to move towards more practical acoustic emission simulations. In this study we mostly focused on showing the capability of the numerical scheme in simulation of acoustic waves induced by local abrupt release of energy in porous media and did not

concentrate on interface constitutive modeling of failure and weakening. This article does not focus on the effectiveness of the methodology in terms of computational costs for large-scale problems. Hence, future research works should focus on solving large scale problems in practical applications like earthquakes and microseismic monitoring in hydraulic fracturing. These work demonstrate a corolation between acoustic events observed in experiments and microscale fracturing and damage processes. Lastly, since in many practical applications AEs are triggered and propagated in three-dimensional spaces, the extension of the current two-dimensional model to three-dimensional would be of great value.

Appendix

$$[M^e]^{11}_{IJ} = \int_{A_e} \rho(\boldsymbol{\psi}^1_I)^\top \boldsymbol{\psi}^1_J d\Omega, \quad [M^e]^{31}_{IJ} = \int_{A_e} \rho_f k_f (\boldsymbol{\psi}^3_I)^\top_{,x} \boldsymbol{\psi}^1_J d\Omega \tag{28}$$

$$[M^e]^{22}_{IJ} = \int_{A_e} \rho(\boldsymbol{\psi}^2_I)^\top \boldsymbol{\psi}^2_J d\Omega, \quad [M^e]^{32}_{IJ} = \int_{A_e} \rho_f k_f (\boldsymbol{\psi}^3_I)^\top_{,y} \boldsymbol{\psi}^2_J d\Omega \tag{29}$$

$$[K^e]^{11}_{IJ} = \int_{A_e} \Big(C_{11} (\boldsymbol{\psi}^1_I)^\top_{,x} (\boldsymbol{\psi}^1_J)_{,x} + C_{33} (\boldsymbol{\psi}^1_I)^\top_{,y} (\boldsymbol{\psi}^1_J)_{,y} \Big) d\Omega, \tag{30}$$

$$[K^e]^{12}_{IJ} = \int_{A_e} \Big(C_{12} (\boldsymbol{\psi}^1_I)^\top_{,x} (\boldsymbol{\psi}^2_J)_{,y} + C_{33} (\boldsymbol{\psi}^1_I)^\top_{,y} (\boldsymbol{\psi}^2_J)_{,x} \Big) d\Omega, \tag{31}$$

$$[K^e]^{13}_{IJ} = \int_{A_e} -\alpha_p (\boldsymbol{\psi}^1_I)^\top_{,x} (\boldsymbol{\psi}^3_J) d\Omega, \tag{32}$$

$$[K^e]^{21}_{IJ} = \int_{A_e} \Big(C_{21} (\boldsymbol{\psi}^2_I)^\top_{,y} (\boldsymbol{\psi}^1_J)_{,x} + C_{33} (\boldsymbol{\psi}^2_I)^\top_{,x} (\boldsymbol{\psi}^1_J)_{,y} \Big) d\Omega, \tag{33}$$

$$[K^e]^{22}_{IJ} = \int_{A_e} \Big(C_{22} (\boldsymbol{\psi}^2_I)^\top_{,y} (\boldsymbol{\psi}^2_J)_{,y} + C_{33} (\boldsymbol{\psi}^2_I)^\top_{,x} (\boldsymbol{\psi}^2_J)_{,x} \Big) d\Omega, \tag{34}$$

$$[K^e]^{23}_{IJ} = \int_{A_e} -\alpha_p (\boldsymbol{\psi}^2_I)^\top_{,y} (\boldsymbol{\psi}^3_J) d\Omega, \tag{35}$$

$$[K^e]^{33}_{IJ} = \int_{A_e} k_f \Big((\boldsymbol{\psi}^3_I)^\top_{,x} (\boldsymbol{\psi}^3_J)_{,x} + (\boldsymbol{\psi}^3_I)^\top_{,y} (\boldsymbol{\psi}^3_J)_{,y} \Big) d\Omega, \tag{36}$$

$$[C^e]^{31}_{IJ} = \int_{A_e} \alpha_p (\boldsymbol{\psi}^3_I)^\top (\boldsymbol{\psi}^1_J)_{,x} d\Omega, \tag{37}$$

$$[C^e]^{32}_{IJ} = \int_{A_e} \alpha_p (\boldsymbol{\psi}^3_I)^\top (\boldsymbol{\psi}^2_J)_{,y} d\Omega, \tag{38}$$

$$[C^e]^{33}_{IJ} = \int_{A_e} (\boldsymbol{\psi}^3_I)^\top (\boldsymbol{\psi}^3_J) \frac{1}{Q} d\Omega, \tag{39}$$

$$\mathbf{F}^e_{Iu_x} = \int_{A_e} \Big(\rho(b_x)(\boldsymbol{\psi}^1_I)^\top\Big) d\Omega +$$

$$\int_{s^t_e} \Big(\bar{t}_x(\boldsymbol{\psi}^1_I)^\top\Big) d\Gamma_t + \int_{s^d_e} \Big(\bar{t}_{d_x}(\boldsymbol{\psi}^1_I)^\top\Big) d\Gamma_d, \tag{40}$$

$$\mathbf{F}^e_{Iu_y} = \int_{A_e} \Big(\rho(b_y)(\boldsymbol{\psi}^2_I)^\top\Big) d\Omega +$$

$$\int_{s^t_e} \Big(\bar{t}_y(\boldsymbol{\psi}^2_I)^\top\Big) d\Gamma_t + \int_{s^d_e} \Big(\bar{t}_{d_y}(\boldsymbol{\psi}^2_I)^\top\Big) d\Gamma_d, \tag{41}$$

$$\mathbf{F}^e_{Ip} = \int_{A_e} k_f \rho_f \Big((\boldsymbol{\psi}^3_I)^\top_{,x} b_x + (\boldsymbol{\psi}^3_I)^\top_{,y} b_y\Big) d\Omega - \int_{s^w_e} \Big(\dot{w} \cdot n_{\Gamma w} (\boldsymbol{\psi}^3_I)^\top\Big) d\Gamma_w \tag{42}$$

in which e is either 1 or 2 for the superimposed elements one and two, respectively, and s^t_e, s^d_e, and s^w_e are the portions of superimposed element e on the traction boundary Γ_t, discontinuity surface Γ_d, and fluid flux boundary Γ_w, respectively. $\bar{t}_{d_x}$ and $\bar{t}_{d_y}$ are the components of contact tractions in x and y directions, respectively.

Acknowledgements

The authors gratefully acknowledge the support of a Discovery Grant, and a Strategic Grant from the Natural Sciences and Engineering Research Council of Canada (NSERC) and an Early Researcher Award from the Ontario Ministry of Innovation and Research.

References

[1] Lockner D., The role of acoustic emission in the study of rock fracture. *Int. J. Rock Mech. Min. Sci. Geomech. Abstr.*, 30(7), 883–899 (1993).

[2] Carpinteri A. , Xu J., Lacidogna G., Manuello A., Reliable onset time determination and source location of acoustic emissions in concrete structures. *Cement & Concrete Composites*, 34, 529–537 (2012).

[3] Xu J., Fu Z., Han Q., Lacidogna G., Carpinteri A. , Micro-cracking monitoring and fracture evaluation for crumb rubber concrete based on acoustic emission techniques. *Structural Health Monitoring*, 1475921717730538 (2017).

[4] Han Q. , Xu J., Carpinteri A., Lacidogna G., Localization of acoustic emission sources in structural health monitoring of masonry bridge. *Structural Control and Health Monitoring*, 22, 314–329 (2015).

[5] Pettitt S., Baker C., Young R., Dahlstrom L.-O. & Ramqvist, G., The assessment of damage around critical engineering structures using induced seismicity and ultrasonic techniques. *Pure appl. Geophys.*, 159(13), 179–195 (2002).

[6] Smith M. B., Montgomery C., Hydraulic fracturing, *CRC Press* (2015).

[7] Warpinski N.R., Mayerhofer M., Agarwal K., Du J., Hydraulic-fracture geomechanics and microseismic-source mechanisms. *SPE Journal*, 18(04), 766–780 (2013).

[8] Invernizzi S., Lacidogna G. and Carpinteri A., Scaling of fracture and acoustic emission in concrete. *Magazine of Concrete Research*, 65(9), 529–534 (2013).

[9] Invernizzi, S., Lacidogna, G. and Carpinteri, A., Particle-based numerical modeling of AE statistics in disordered materials. *Magazine of Concrete Research*, 48(1), 211–220 (2013).

[10] Invernizzi S., Lacidogna G. and Carpinteri A., Numerical Models for the Assessment of Historical Masonry Structures and Materials, Monitored by Acoustic Emission. *Applied Sciences*, 6(4), 102 (2016).

[11] Carpinteri A., Lacidogna G., Corrado M. and Di Battista E., Cracking and crackling in concrete-like materials: A dynamic energy balance. *Engineering Fracture Mechanics*, 155, 130–144 (2016).

[12] Tang C., Numerical simulation of progressive rock failure and associated seismicity. *Int. J. Rock Mech. Min. Sci.*, 34(2), 249–261 (1997).

[13] Tang C.A., Kaiser P.K., Numerical simulation of cumulative damage and seismic energy release during brittle rock failurepart I: fundamentals. *Int. J. Rock Mech. Min. Sci.*, 35(2), 113–121 (1998).

[14] Hazzard, J., Young, R., Simulating acoustic emissions in bonded-particle models of rock. *Int. J. Rock Mech. Min. Sci.*, 37(5), 867–872 (2000).

[15] Lisjak A., Liu Q., Zhao Q., Mahabadi O. K., Grasselli G., Numerical simulation of acoustic emission in brittle rocks by two-dimensional finite-discrete element analysis. *Geophysical Journal International*,

195(1), 423–443 (2013).

[16] Pearson C., The relationship between microseismicity and high pore pressures during hydraulic stimulation experiments in low permeability granitic rocks. *Journal of Geophysical Research*, 86, 7855–7864 (1981).

[17] Iturrioz I., Lacidogna G., Carpinteri A., Experimental analysis and truss-like discrete element model simulation of concrete specimens under uniaxial compression. *Engineering Fracture Mechanics*, 110, 81–98 (2013).

[18] Birck G., Iturrioz I., Lacidogna G., Carpinteri A., Damage process in heterogeneous materials analyzed by a lattice model simulation. *Engineering Failure Analysis*, 70, 157–176 (2016).

[19] Andreykiv O.Y., Lysak M.V., Serhiyenko O.M., Skalsky V.R., Analysis of acoustic emission caused by internal cracks. *Eng. Fract. Mech.*, 68(11), 1317–1333 (2001).

[20] Andreykiv O., Skalsky V., Serhiyenko O., Rudavskyy D., Acoustic emission estimation of crack formation in aluminium alloys. *Eng. Fract. Mech.*, 77(5), 759–767 (1010).

[21] Nazarchuk Z., Skalskyi V. and Serhiyenko O., Acoustic Emission: Methodology and Application, *Springer* (2017).

[22] Jha B, Juanes R, A locally conservative finite element framework for the simulation of coupled flow and reservoir geomechanics. *Acta Geotechnica*, 2(3), 139–153 (2007).

[23] Moeendarbary E, Valon L, Fritzsche M, Harris AR, Moulding DA, Thrasher AJ, Stride E, Mahadevan L, Charras GT, The cytoplasm of living cells behaves as a poroelastic material. *Nat Mater*, 12(3), 253261 (2013).

[24] Fraldi M, Carotenuto A R, Cells competition in tumor growth poroelasticity. *Journal of the Mechanics and Physics of Solids*, 112(3), 345–367 (2018).

[25] Cao T. D., Hussain F., Schrefler B. A., Porous media fracturing dynamics: stepwise crack advancement and fluid pressure oscillations, *Journal of the Mechanics and Physics of Solids*, 111, 113–133 (2018).

[26] Rethore J., De Borst R., Abella M.A., A discrete model for the dynamic propagation of shear bands in a fluidsaturated medium. *International journal for numerical and analytical methods in geomechanics*, 31(2), 347–370 (2007).

[27] Bathe K. J., Finite element procedures, *Prentice Hall* (1996).

[28] Ham S., Bathe K. J., A finite element method enriched for wave propagation problems, *Computers & Structures*, 94-95, 1–12 (2012).

[29] Kohno H., Bathe K. J., Wright J. C., A finite element procedure for multiscale wave equations with application to plasma waves. *Computers & Structures*, 88, 8794 (2010).

[30] Komijani M, Gracie R., An enriched finite element model for wave propagation in fractured media,

Finite Elements in Analysis and Design, 125, 14–23 (2017).

[31] Jeong-Hoon Song, Pedro M. A. Areias, Belytschko T., A method for dynamic crack and shear band propagation with phantom nodes. *International Journal for Numerical Methods in Engineering*, 67, 868893 (2006).

[32] Yoon Y. C., Song J. H., Extended particle difference method for moving boundary problems. *Computational Mechanics*, 54, 723–743 (2014).

[33] Yoon Y. C., Song J. H., Extended particle difference method for weak and strong discontinuity problems: part I. Derivation of the extended particle derivative approximation for the representation of weak and strong discontinuities. *Computational Mechanics*, 53(6), 1087–1103 (2014).

[34] Yoon Y. C., Song J. H., Extended particle difference method for weak and strong discontinuity problems: part II. Formulations and applications for various interfacial singularity problems. *Computational Mechanics*, 53(6), 11051128 (2014).

[35] Terzaghi K., Theoretical soil mechanics. *Wiley: New York*, (1943).

[36] Biot M.A., Mechanics of incremental deformations. *Wiley: Chichester*, (1965).

[37] Zienkiewicz OC, Chan AHC, Pastor M, et al, Computational Geomechanics with Special Reference to Earthquake Engineering, *John Wiley & Sons, Inc, New York* (1999).

[38] Ji H., Dolbow J. E., On strategies for enforcing interfacial constraints and evaluating jump conditions with the extended finite element method. *International Journal for Numerical Methods in Engineering*, 61(14), 2508–2535 (2004).

[39] Moës N., Béchet E., Tourbier M., Imposing Dirichlet boundary conditions in the extended finite element method. *International Journal for Numerical Methods in Engineering*, 67(12), 1641–1669 (2006).

[40] Hautefeuille M., Annavarapu C., Dolbow J.E., Robust imposition of Dirichlet boundary conditions on embedded surfaces. *International Journal for Numerical Methods in Engineering*, 90(1), 40–64 (2012).

[41] Khoei, A.R., Extended finite element method: theory and applications. *John Wiley & Sons*, (2014).

[42] Komijani M, Gracie R., Enriched Mixed Finite Element Models for Dynamic Analysis of Continuous and Fractured Porous Media, *Computer Methods in Applied Mechanics and Engineering*, Under publication (2018).

- Presentation of improved methods for the simulation of acoustic emission in fracture porous media.

- Presentation of the first application of the combination of the Phantom Node Method (PNM) and Generalized Finite Element Method (GFEM) to model instability induced wave propagation in fractured porous media.

- Illustration that GFEM enrichment with suitable trigonometric functions can significantly reduce the spurious oscillations which appear in FEM simulations of acoustic emission.

- Presentation of an Augmented Lagrangian Method to implement contact and stick-slip friction between fracture surfaces, in the context of the PNM and the PNM-GFEM-M for simulation of fracture reactivation.